Structure
Article

The Human Breast Cancer Resistance Protein (BCRP/ABCG2) Shows Conformational Changes with Mitoxantrone

Mark F. Rosenberg,[1,*] Zsolt Bikadi,[2,3] Janice Chan,[1] Xiaoping Liu,[2] Zhanglin Ni,[2] Xiaokun Cai,[2] Robert C. Ford,[1] and Qingcheng Mao[2]
[1]Manchester Interdisciplinary Biocentre, 131 Princess Street, University of Manchester, Manchester, M1 7DN, UK
[2]Department of Pharmaceutics, School of Pharmacy, University of Washington, Seattle, WA 98195, USA
[3]Virtua Drug Ltd., Csalogany Street 4, H-1015 Budapest, Hungary
*Correspondence: mark.rosenberg@manchester.ac.uk
DOI 10.1016/j.str.2010.01.017

SUMMARY

BCRP/ABCG2 mediates efflux of drugs and xenobiotics. BCRP was expressed in *Pichia pastoris*, purified to > 90% homogeneity, and subjected to two-dimensional (2D) crystallization. The 2D crystals showed a $p12_1$ symmetry and projection maps were determined at 5 Å resolution by cryo-electron microscopy. Two crystal forms with and without mitoxantrone were observed with unit cell dimensions of a = 55.4 Å, b = 81.4 Å, γ = 89.8°, and a = 57.3 Å, b = 88.0 Å, γ = 89.7°, respectively. The projection map without mitoxantrone revealed an asymmetric structure with ring-shaped density features probably corresponding to a bundle of transmembrane α helices, and appeared more open and less symmetric than the map with mitroxantrone. The open and closed inward-facing forms of BCRP were generated by homology modeling, representing the substrate-free and substrate-bound conformations in the absence of nucleotide, respectively. These models are consistent with the experimentally observed conformational change upon substrate binding.

INTRODUCTION

Resistance to anticancer agents is a major cause of chemotherapeutic failure in cancer. One mechanism involves active extrusion of drugs out of cells by membrane transport proteins resulting in cellular drug levels below that required for cytotoxicity. Clinical and in vitro cell-based studies have shown that multidrug resistance is often associated with increased expression of one or more transport proteins belonging to the ATP-binding cassette (ABC) transporter superfamily which use the energy provided by ATP binding and hydrolysis at their nucleotide binding domains (NBDs) to transport substrates across the cell membrane (Sarkadi et al., 2006). The most important eukaryotic ABC transporters involved in multidrug resistance are P-glycoprotein (P-gp/ABCB1), multidrug resistance protein 1 (MRP1/ABCC1), and breast cancer resistance protein (BCRP/ABCG2).

The 75 kDa human BCRP is a polytopic plasma membrane transport protein that has been detected in many drug-resistant cell lines, solid tumors, and hematological malignancies (Robey et al., 2009). Transport studies using BCRP-overexpressing intact cells or BCRP-enriched plasma membrane vesicles have established that BCRP can actively transport a broad spectrum of substrates, ranging from hydrophobic chemotherapeutics to hydrophilic anionic conjugated endo- and xenobiotics (Mao and Unadkat, 2005; Polgar et al., 2008). BCRP is highly expressed in organs important for the absorption (the small intestine), distribution (e.g., the blood-brain and placental barriers), and elimination (e.g., the liver and kidney) of drugs (Maliepaard et al., 2001), and plays an important role in drug disposition (Mao and Unadkat, 2005; Robey et al., 2009).

ABC transporters usually consist of two hydrophobic transmembrane domains (TMDs) with 12 transmembrane (TM) α helices and two hydrophilic NBDs for substrate and ATP binding, respectively (Sarkadi et al., 2006). P-gp and MRP1 are arranged in two repeated halves with 12 and 17 TM α helices, respectively, forming a funnel facing the outside of cell membrane (Loo and Clarke, 2001; Rosenberg et al., 2005) and a higher resolution structure of P-gp was recently described (Aller et al., 2009). In contrast, BCRP is a half ABC transporter with one NBD followed by one TMD (Polgar et al., 2008). The most recent topology analysis suggests that the TMD of BCRP consists of 6 TM α helices (Wang et al., 2008). Hence, BCRP appears to require homodimerization to exert its activity and a homotetrameric configuration of BCRP has been proposed (McDevitt et al., 2006; Xu et al., 2004). The substrate specificity of BCRP is overlapping with, but distinct from that of P-gp and MRP1 (Mao and Unadkat, 2005; Polgar et al., 2008). TM6 and TM12 of P-gp are involved in drug binding (Loo and Clarke, 2001). It has been shown that arginine at position 482 of BCRP, which is located within TM3 near the cytosolic membrane interface, is critical for substrate specificity and transport activity, suggesting that an alternative drug-binding mechanism is applicable for BCRP (Honjo et al., 2001; Ozvegy-Laczka et al., 2005).

Structural features responsible for such differences in drug-binding and transport mechanisms of different ABC transporters are yet not known. Indeed, little is known about the structure

of BCRP, although an atomic model of BCRP was recently predicted by homology modeling based on the crystal structure of the bacterial multidrug exporter Sav1866, which suggested that BCRP had multiple drug-binding sites (Hazai and Bikadi, 2008). We have previously reported functional expression of human BCRP at a relatively high level in *Pichia pastoris* (Mao et al., 2004). BCRP expressed in *Pichia pastoris* was active in transporting its substrate estrone 3-sulfate and in hydrolyzing ATP. This suggested that *Pichia pastoris* could be used to overexpress and purify BCRP for structural analysis. In this study, we have purified BCRP from *Pichia pastoris*, facilitated by a 10-histidine tag attached to the COOH-terminus of the transporter. Electron crystallography has emerged as a powerful tool to determine the structures of membrane proteins from 2D crystals, including that of P-gp (Rosenberg et al., 2005) and several at atomic resolutions (Gonen et al., 2005; Holm et al., 2006; Kuhlbrandt et al., 1994). We have captured structural information of BCRP from 2D crystals that were grown in the presence and absence of the substrate drug mitoxantrone, analyzed by cryo-electron microscopy (cryo-EM), and projection structures determined at 5 Å resolution. Conformational changes were observed in 2D crystals grown in the absence and presence of mitoxantrone. Analysis and homology modeling of the differences between these structural states also indicated a significant conformational change. This structural information provides a basis for further structural and mechanistic analysis of BCRP and related ABC proteins.

RESULTS AND DISCUSSION

Production and Characterization of BCRP Expressed in *Pichia pastoris*

Recombinant full-length human BCRP with a 10-histidine tag attached at the COOH-terminus of the protein was expressed in *Pichia pastoris* as previously described (Mao et al., 2004). The expression of BCRP in *Pichia pastoris* was detected by immunoblotting of the microsomes with the monoclonal antibody BXP-21 and a major immunoreactive band of approximately 65 kDa was observed (Figure 1A). Solubilization of BCRP from crude microsome membranes was evaluated using several detergents. Approximately 50% of BCRP was solubilized by lysophosphatidylcholine (LPC) at a LPC/protein ratio (mg/mg) of more than 5. N-dodecyl β-D maltoside (DDM) was more effective than LPC, which solubilized more than 90% of BCRP at a relatively low DDM/protein ratio (mg/mg) of 2 at 4°C.

The detergent extract of BCRP was subjected to Ni^{2+}-NTA affinity chromatography. Comparison of the detergent-extract and flow through suggested that more than 70% of the DDM-solubilized BCRP bound to Ni^{2+}-NTA as visualized on silver-stained SDS-PAGE (Figure 1B, lanes 1–3). BCRP was purified to more than 90% homogeneity visualized as an approximately 65 kDa full-length underglycosylated protein with no apparent contaminating bands (Figure 1B, lanes 4–8). An immunoblot confirmed that these bands were BCRP (data not shown). Further purification by anion exchange chromatography was precluded because the protein was thought to be sufficiently pure. The overall yield of BCRP purified from 1.0 l yeast culture was approximately 200 μg. This BCRP preparation was suitable for electron crystallography by growing the crystals directly on the surface of an electron microscope (EM) grid, which requires less protein (Rosenberg et al., 2005).

Purified BCRP in detergent solution was active in hydrolyzing ATP with a basal activity of approximately 20–60 nmol Pi/min/mg protein (Figures 1C and 1D), which could be modulated by prazosin (Figure 1E), a known BCRP substrate that has been shown to stimulate BCRP ATPase activity (Glavinas et al., 2007). This finding suggests that the purified BCRP remains correctly folded in a nonreconstituted environment and the protein had retained its activity through the purification process. The relatively low basal ATPase activity of BCRP was likely due to BCRP presenting in a nonreconstituted membrane environment, but was in a similar range of the ATPase activity of BCRP purified from insect cells (Pozza et al., 2006).

Two-Dimensional Crystals of BCRP in Different Conformational States

Well-ordered 2D crystals of BCRP were grown in the presence of DDM as previously described (Rosenberg et al., 2005), except that the crystals here were grown directly on the surface of continuous carbon/molybdenum or carbon/gold grids at 4°C. In general, the crystals were larger and better ordered than the P-gp crystals and thus more suitable for structure analysis by electron crystallography (Figure 2). These crystals were sometimes 1.5 μm in width and 1.5 μm in length, and appeared visually different to those of P-gp (Rosenberg et al., 2003) and CFTR (Rosenberg et al., 2004), having less of a "honeycomb" and a more of "square-shaped" appearance suggesting a different space group compared with P-gp and CFTR (see below). The crystals were grown in the presence or absence of 5 mM mitoxantrone by adding this drug to the appropriate crystallization droplet.

The crystals were initially negatively stained, but to extend the resolution of the data, cryo-EM was undertaken (Rosenberg et al., 2005). Two different types of crystal forms were observed. The calibrated unit cell parameters for the monoclinic type crystal form in the absence of mitoxantrone were a = 57.3 ± 0.7 Å (n = 5), b = 88.0 ± 0.95 Å (n = 5), γ = 89.7 ± 0.6° (n = 5), while the other crystal form in the presence of mitoxantrone measured a = 55.4 ± 0.6 Å (n = 5), b = 81.4 ± 1.1 Å (n = 5), γ = 89.8 ± 0.5° (n = 5) (Table 1). In general, the crystals in the presence of the drug were larger and better ordered than the crystals in the absence of the drug. This significant change in unit cell dimensions, especially in the b direction, suggests that the crystal packing has changed in the presence of mitoxantrone and BCRP has adopted different conformations. Recent studies for NhaA, the Na^+/H^+ exchanger from *E. coli*, also demonstrated changes in unit cell dimensions concomitant with conformational changes and showed that one crystal form was better ordered than the other (Appel et al., 2009). The 2D crystals of BCRP had a two-sided plane group $p12_1$ symmetry determined by ALLSPACE (Valpuesta et al., 1994). Gamma (γ) could have been very slightly less than the required 90 degree angle for this space group because of a slight crystal tilt on the electron microscope grid for both mitoxantrone and non-mitoxantrone crystal forms (Valpuesta et al., 1994). This space group is different to that for P-gp and CFTR.

Low-dose images of frozen-hydrated crystals preserved in ice showed strong reflections at ~8 Å by optical diffraction. After

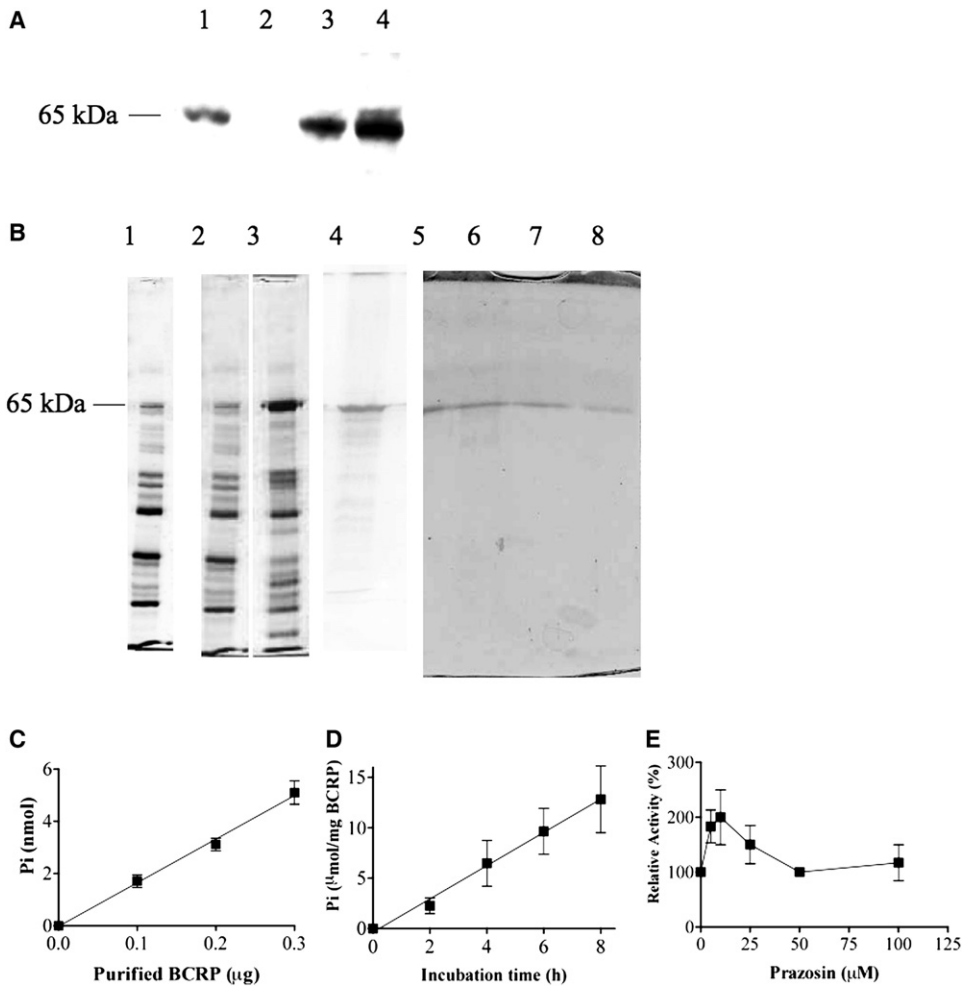

Figure 1. Expression, Purification, and ATPase Activity of BCRP

BCRP was expressed in *Pichia pastoris* and purified as described.

(A) Immunoblot of BCRP-enriched crude microsome membranes (20 μg of protein each lane) isolated from *Pichia pastoris* cells. Lanes 1, 3, and 4 indicate the membrane preparations from different batches of cells expressing BCRP. Lane 2 represents the membranes prepared from the control cells with no BCRP expression.

(B) Purification of BCRP by Ni^{2+}-NTA affinity chromatography was monitored by analyzing protein samples on 10% SDS-PAGE followed by silver staining in lanes 1–4 and Coomassie blue staining in lanes 5–8. Lane 1, flow-through from Ni^{2+}-NTA column (20 μl); lane 2, eluate from the first wash of Ni^{2+}-NTA column with resuspension buffer (20 μl); lane 3, eluate with 100 mM imidazole (20 μl); lanes 4–8, sequential fractions of eluates with 200 mM imidazole (20 μl each). Either silver staining or Coomassie blue staining revealed a clearly enriched BCRP band at approximately 65 kDa in lanes 4 –8.

(C) ATPase activity measured at 37°C with various amounts of purified BCRP in the absence of prozosin for 4 hr.

(D) Time-dependence of ATPase activity determined at 37°C with 0.2 μg purified BCRP.

(E) The effect of prazosin at various concentrations on ATPase activity measured at 37°C with 0.2 μg purified BCRP for 2 hr. Shown are means ± standard deviations (SDs) of three independent determinations.

correction for lattice distortions, the crystals in the presence of mitoxantrone yielded structure factors to 4.0 Å resolution (Figure 3A). In the absence of mitoxantrone, the crystals were slightly less well ordered; however, the corresponding deviation map (see Figure S1 available online) of the 2D crystals with vectors (magnified 20×) between the perfect adapted lattice and the actual unit cell positions suggests that the drug-free crystals are also well ordered, especially in the center of the crystals. A plot of the phase quality shows that these crystals extend to 8 Å resolution (data not shown). For these crystals the Mathews coefficient calculated with CCP4 (CCP4, 1994) suggested that there were 4 BCRP monomers (two BCRP dimers) in the asymmetric unit cell assuming that the molecular mass of each BCRP monomer was 65 kDa. McDevitt et al. (McDevitt et al., 2006) reported a tetrameric 3D structure for BCRP purified from insect cells in which different detergents were used for extraction and purification of BCRP. It has been documented that the association state of membrane proteins can depend on the detergent used (Larue et al., 2009). However, both the projection maps of this study and the previously reported 3D map could be consistent with a tetrameric structure because the tetramer would consist of four homodimeric BCRP molecules.

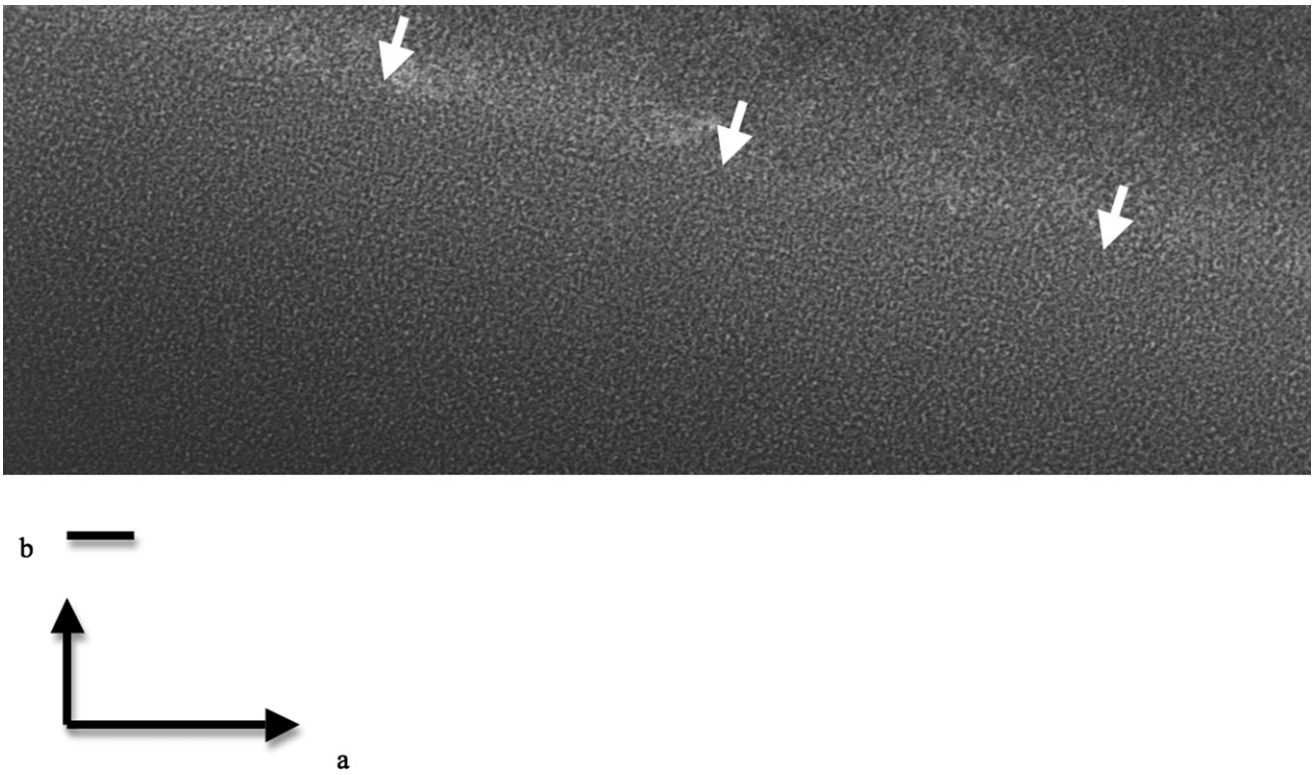

Figure 2. Negatively Stained 2D Crystals of BCRP of the $p12_1$-Type Stained with 2% (w/v) Uranyl Acetate
Arrows indicate 2D crystals of BCRP of the $p12_1$ type in the absence of mitoxantrone. The 2D crystals of BCRP with mitoxantrone looked similar to those without mitoxantrone (data not shown). Scale bar represents 123 nm. See also Figure S1.

Projection maps of 2D crystals of BCRP in the presence and absence of mitoxantrone with data truncated at 5 Å resolution and a $p12_1$ symmetry enforced were calculated after merging data from six and five independent lattices, respectively (Figure 4). The overall average phase residual was 35° and 25° for the drug-free and drug-bound crystal forms, respectively (Table 1). A single crystal image exhibited a screw axis, providing confidence in the assignment of the space group and the value of the Mathews coefficient. In both crystal forms, the unit cell contains two BCRP homodimers related by a two-fold screw axis along b with the dimer being present in alternately up and down orientations. Each homodimer is composed of two polypeptide chains related by a noncrystallographic two-fold axis of rotational symmetry. The BCRP molecules were clearly delineated, but the packing of the dimers is different in the two crystal forms. The BCRP dimers in the presence of mitoxantrone were rotated ~20° relative to the no-drug crystal form, resulting in a closer inter-dimer packing (Figure 4B). The introduction of additional close contacts between the BCRP dimers presumably resulted in a better crystalline order in the presence of the drug. Consequently, the shape of the BCRP molecules was different between the two maps, with the BCRP molecules having a more closed configuration in the presence of mitoxantrone (Figure 4B) and a more open shape in the absence of the drug (Figure 4A). A difference map between the drug-free and drug-bound forms was calculated (Figure S2). The main changes appear to be a small solid body rotation around the crystal normal and, as implied by the unit cell parameters, a compression of the structure in the presence of mitoxantrone. These data suggest that, in the presence of mitoxantrone, BCRP has undergone a significant conformational change. This seems to fit with the interpretation in the models of a drug-induced closing up of the transporter, which has implications for the mechanisms of ABC transporters in general (see below).

For X-ray structures of the bacterial ABC lipid transporter, MsbA, trapped in different conformations, two nucleotide-bound structures and two in the absence of nucleotide, were recently reported (Ward et al., 2007). The two nucleotide-bound structures share the same outward-facing conformation, whereas the two nucleotide-free apo structures have different inward-facing conformations. The TMDs of MsbA are much closer in the closed apo conformation than in the open apo conformation. These authors suggested that the closed apo conformation might represent an intermediate conformation between the open apo and the nucleotide-bound outward-facing conformations, and that substrate binding to the open apo conformation may promote the closure of the TMDs of MsbA, which would, in turn, send a signal to the NBDs, allowing the formation of the ATP sandwich upon nucleotide binding. The finding of this study that the projection maps of BCRP display a more closed conformation in the presence of mitoxantrone and a more open shape in the absence of the drug appears to be consistent with the structural data of MsbA.

Table 1. Crystallographic Image Processing Data for 2D Crystals of BCRP

2D Crystals of BCRP in the Absence of Mitoxantrone		
Two-sided plane group symmetry	$p12_1$	
Unit cell parameters	a = 57.3 ± 0.7 Å (n = 5)	
	b = 88.0 ± 0.95 Å (n = 5)	
	γ = 89.7 ± 0.6° (n = 5)	
Number of crystals used for merging	5	
Number of observations, IQ[a] ≤ 7	320	
Overall phase residual to 6 Å, IQ ≤ 5	35°	
	Phase residual	
Resolution range (Å)	Number of observations	Phase residual (random = 90°)
200 – 18	24	38.9°
20 – 14	13	34.6°
15 – 9.5	42	38.2°
10 – 8	32	36.7°
8 – 5.5	70	27.9°
5.5 – 5.1	30	37.7°
2D crystals of BCRP in the presence of mitoxantrone		
Two-sided plane group symmetry	$p12_1$	
Unit cell parameters	a = 55.4 ± 0.6 Å (n = 5)	
	b = 81.4 ± 1.1 Å (n = 5)	
	γ = 89.8 ± 0.5° (n = 5)	
Number of crystals used for merging	6	
Number of observations, IQ ≤ 7	350	
Overall phase residual to 6 Å, IQ ≤ 5	25°	
	Phase residual	
Resolution range (Å)	Number of observations	Phase residual (random = 90°)
200 – 18	20	37.3°
20 – 14	19	40.9°
15 – 10	24	32.7°
10 – 7	35	35.0°
7 – 5.5	42	33.3°
5.5 – 4.1	37	21.0°

[a] IQ is a measure of the signal/noise ratio of reflections.

Each BCRP monomer is predicted to contain 6 TM α helices (Wang et al., 2008). In EM images obtained under cryoconditions, the entire protein contributes to the information contained in the images; thus, the extramembranous features as well as the TM elements may be superimposed in EM projection maps. Long α helices with axes close to the crystal normal could give rise to strong 0.8–1 nm diameter features in the projection map. At approximately 5 Å resolution, the spacing and dimensions of some of the typical strong densities in the BCRP projection maps may be consistent with those of TM α helices (Figure 4). The resolution of the projection maps is not sufficient to interpret any of the densities as arising from re-entrant loops such as those observed in aquaporin (Murata et al., 2000) or those suggested to be present in bacterial transporters, neurotransmitter transporters, and ion exchanger antiporters (Slotboom et al., 1999; Wakabayashi et al., 2000).

Membrane Topology of BCRP

Although a high-resolution 3D structure of BCRP has not been available, homology models of BCRP have been reported (Hazai and Bikadi, 2008; Li et al., 2007). To further understand the interactions between BCRP monomers in the 2D crystals, it would be of value to fit homology models of BCRP to the projection maps we have obtained. However, the currently available homology models do not appear to correctly predict the real structure of BCRP as these models were based on the computer prediction of BCRP topology structure, which is quite different from the experimentally determined topology structure (see below). Moreover, the currently available homology models represent a substrate-free and nucleotide-bound conformation of BCRP, which seems unsuitable to interpret the projection structures of this study obtained with and without a substrate in the absence of nucleotide. Therefore, we first performed relevant homology modeling based on the topology structure of BCRP we recently determined (Wang et al., 2008). A major difference between the experimentally determined topology structure and computer prediction is that the computer-predicted TM2 and TM5 are shifted to the extracellular and intracellular loops in the experimental model, respectively (Wang et al., 2008). To further confirm this significant shift, we generated additional HA-tagged BCRP mutants using HA tag insertion mutagenesis, one at a time, at positions immediately following the residues 435 (construct 435-HA), 445 (construct 445-HA), 460 (construct 460-HA), 470 (construct 470-HA), 540 (construct 540-HA), and 550 (construct 550-HA). Wild-type and HA-tagged mutant BCRP were expressed in HEK cells by transit transfection. Immunoblotting using the BXP-21 antibody detected wild-type BCRP and all the mutants at comparable levels (Figure 5A). When immunoblotting was performed using a monoclonal antibody against the HA tag, immunoreactive bands of approximately 75 kDa were observed for all the mutants, but were absent for the vector control or wild-type BCRP (Figure 5A). These results suggest that all the HA-tagged BCRP mutants were well expressed in HEK cells at levels comparable to wild-type BCRP. Immunofluorescence analysis was then performed with intact cells or cells that had been permeabilized with Triton X-100 to determine extracellular or intracellular location of the HA tags, respectively. No cell-based fluorescence was detected in intact or permeabilized nontransfected control cells (data not shown) or in cells expressing wild-type BCRP (Figure 5B). However, a strong immunofluorescence signal was detected in both intact and permeabilized cells expressing the mutants with HA tag insertions at residues 435 (construct 435-HA) (Figure 5B, b and e) and 445 (construct 445-HA) (Figure 5B, c and f), suggesting the extracellular location of the HA tags at positions 435 and 445. In contrast, cells expressing the mutants with HA tag insertion at residues 540 (construct 540-HA) (Figure 5B, i and m) and 550 (construct 550-HA) (Figure 5B, j and n) showed bright

 ©2010 Elsevier Ltd All rights reserved

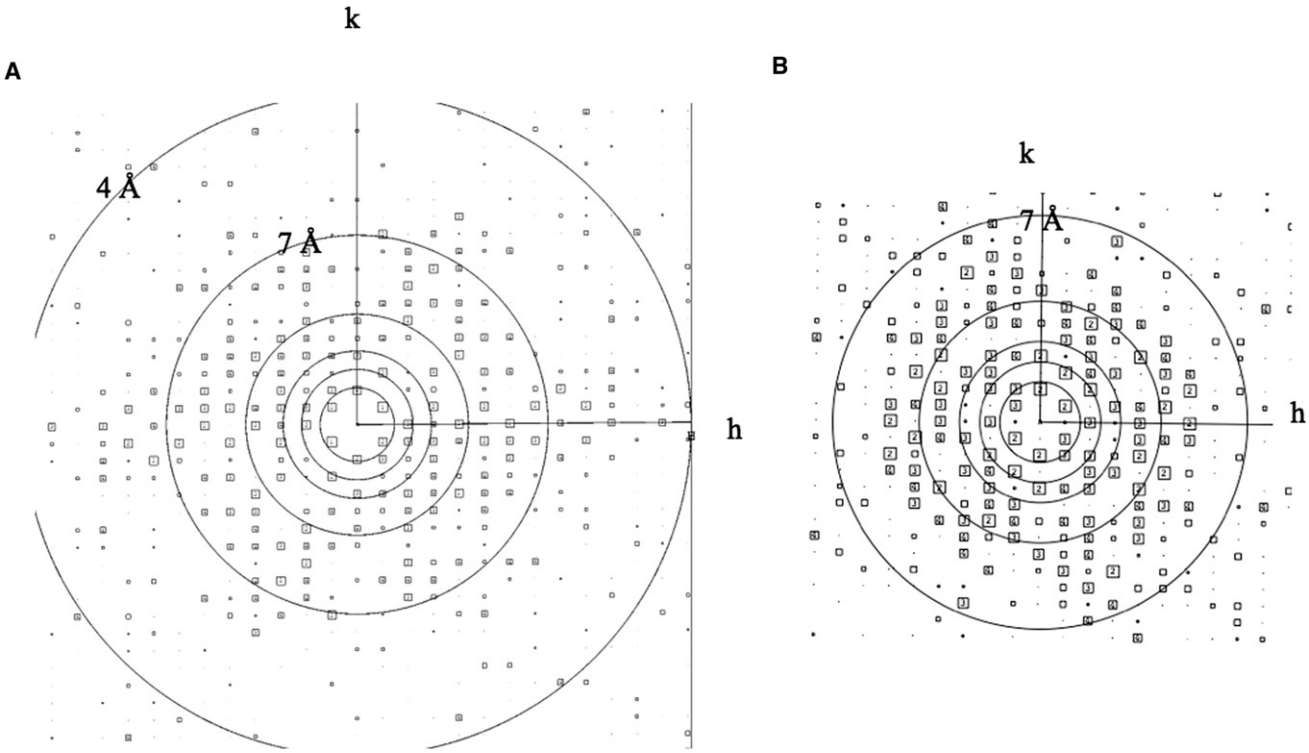

Figure 3. Diffraction Patterns of the BCRP Crystals

Shown are calculated Fourier transform amplitudes from the BCRP crystals after lattice unbending. The size of the squares and the numbers correspond to the IQ value of the spots (Henderson et al., 1986). The rings depict the resolution bins. The axes give the directions of the reciprocal lattice vectors *h* and *k*. The left (A) and the right (B) panels show the diffraction patterns of 2D crystals of BCRP in the presence and absence of 5 mM mitoxantrone, respectively. In the presence of mitoxantrone, the data extended to 4 Å resolution in one direction.

fluorescence only in permeabilized cells, but not in intact nonpermeabilized cells. This demonstrates the intracellular location of the HA tags at positions 540 and 550. The fluorescence signal associated with the mutants with HA tag insertion at residues 460 (construct 460-HA) (Figure 5B, g) and 470 (construct 470-HA) (Figure 5B, h) was rather weak, and could be barely detected only in permeabilized cells, suggesting that the HA tag at these positions is located in a region with limited accessibility to the antibody. Thus, the residues 460 and 470 are likely located in a TM segment. For all the mutants, fluorescence staining was mainly observed in the plasma membrane (Figure 5B), suggesting that these mutants were predominantly targeted to the plasma membrane of HEK cells. These immunoblotting and confocal microscope data indicate that HA tag insertion in all of the mutants does not appear to cause a major alteration in BCRP structure that can affect protein stability, expression, folding, and targeting to the plasma membrane. The mitoxantrone efflux activity of the mutants were approximately 11.7%, 3.6%, 4.2%, 15.3%, 9.7%, and 34.0% of wild-type BCRP activity for constructs 435-HA, 445-HA, 460-HA, 470-HA, 540-HA, and 550-HA, respectively (data not shown). The activity data indicate that, except for constructs 445 and 460, other mutants retained at least partial transport activity, confirming that sufficient amounts of these mutants were correctly folded and targeted to the plasma membrane to exert efflux activity. The decreased activities may reflect functional importance of the positions at which the tag is inserted, rather than major structural alterations. Taken together, these data further support the topology structure of BCRP we previously reported (Wang et al., 2008). As shown in Figure 5C, the residues 431–450 which were predicted to be part of TM2 were now found to be in an extracellular region, whereas residues 460, 462, and 470 that were predicted in an intracellular loop were determined to be in the TM2. The residues 562–582 predicted to be in an extracellular loop were determined to form the TM5. The computer-predicted TM1, TM3, TM4, and TM6 are in correspondence with the experimental data.

Homology Modeling of BCRP

Our earlier BCRP model (Hazai and Bikadi, 2008) was constructed using the Sav1866 structure (Dawson and Locher, 2006) as template and reflects the nucleotide-bound outward-facing conformation. Owing to the low amino acid identity particularly in the TMDs among ABC transporters, the membrane topology of BCRP used in our previous study was primarily based on computer predictions. However, our experimental data clearly indicate that there are crucial differences between the predicted and the experimentally determined topology structures. Except for two regions, the overall topology structure of BCRP deduced from the experimental data is surprisingly similar to that of P-gp observed in its X-ray structure (Aller et al., 2009) (Figure 5C). First, the relatively large intracellular

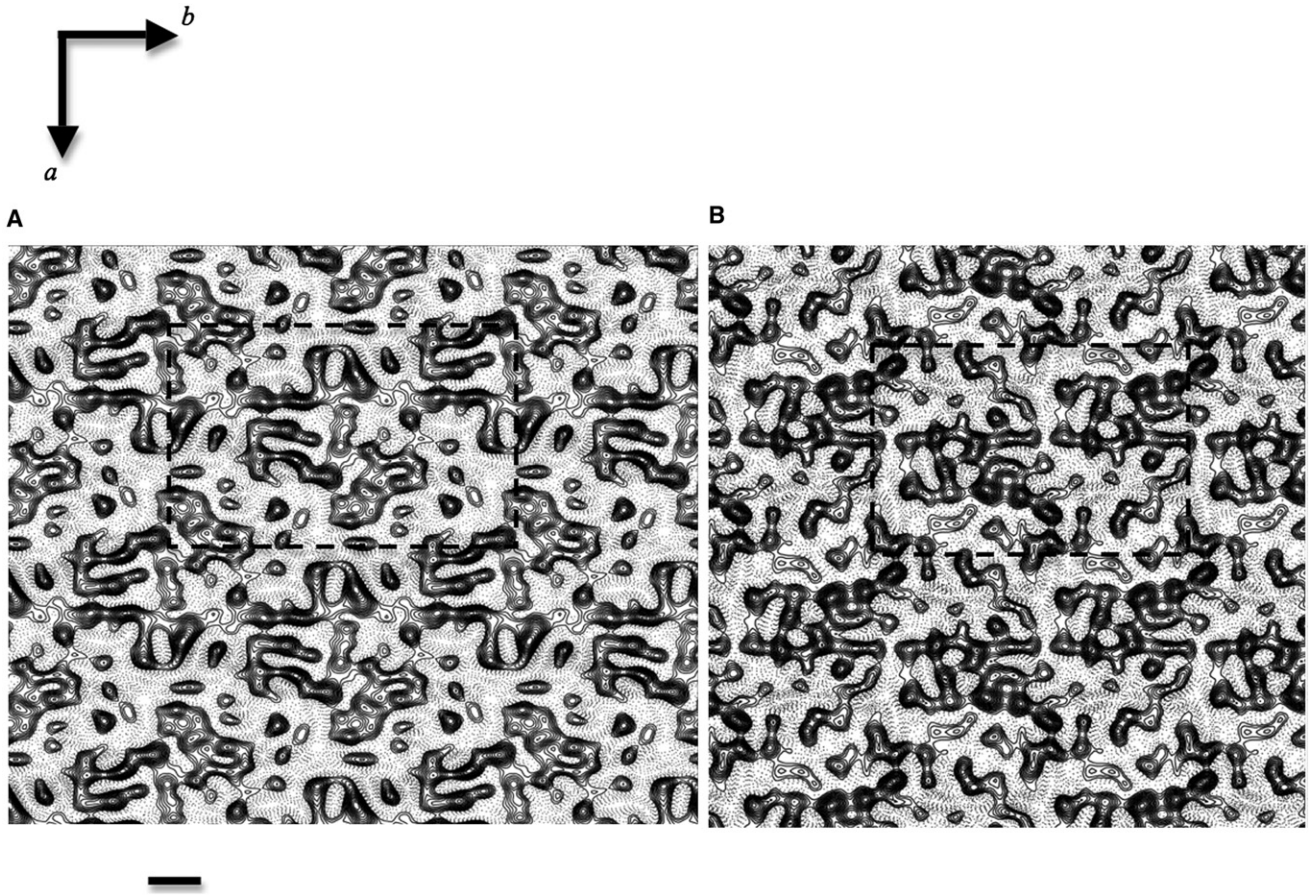

Figure 4. Projection Maps of 2D Crystals of BCRP at 5 Å Resolution

Shown are projection maps of 2D crystals of BCRP at 5 Å resolution in the absence (A) and presence (B) of mitoxantrone under cryoconditions. One unit cell is outlined by the boxes in the projection maps. The maps were calculated from merged amplitudes and phases from five or six independent lattices of crystals embedded in vitreous ice drawn in $p12_1$. Dashed contours represent density below the mean, and solid contours represent density above the mean. The contour interval is at about one-third of the root-mean-square density. Typical strong density peaks in the projection maps are evident (see Discussion). Scale bar represents 13 Å. See also Figure S2.

loop connecting TM2 and TM3 that contains a coupling helix to interact with the NBD of the same monomer as seen in the X-ray structures of P-gp, Sav1866, and MsbA is missing in BCRP. As a result, TM3 of BCRP is rather short and does not intrude into the intracellular loop. Second, the extracellular loop connecting TM5 and TM6 of BCRP is significantly longer than the corresponding region in P-gp. Figure S3 shows a multiple sequence alignment between the templates used for homology modeling and BCRP based on the experimentally determined topology. The order of TMD and NBD of the templates was switched to reflect that of BCRP and the linker region was deleted. The resulting sequence alignment suggests that the number of gaps is considerably lower and the amino acid identity in the TMD is much greater than that of sequence alignments solely based on TM computer predictions (Hazai and Bikadi, 2008; Li et al., 2007). The overall amino acid identity between the TMDs of BCRP and the first half of mouse P-gp is approximately 18% without gaps. Furthermore, most of the putative TM α helices of BCRP start and/or end with glycine or proline (Figure 5C; Figure S3), similar to that observed for P-gp. Residues that form the TMs are mostly hydrophobic, whereas the intracellular and extracellular loops contain more hydrophilic residues. The relative high amino acid identity in the TMDs and the pattern of residue distribution suggest a good quality of the sequence alignment. Li et al. (Li et al., 2007) were unable to find adequate sequence identity between P-gp and BCRP. This is likely due to the major shifts in our experimentally determined topology. For example, the large intracellular loop connecting TM2 and TM3 in the computer-predicted topology does not exist in our experimental topology model. We found that, based on the experimental topology model, the amino acid identity between the TMDs of P-gp and BCRP was much improved.

The homology model using the MsbA structure as template (Protein Data Bank [PDB] code 3B5W) (Ward et al., 2007) generated the substrate-unbound nucleotide-free apo inward-facing conformation of BCRP (Figure 6A). The structure of the NBD is well conserved among ABC transporters and has been extensively discussed (Li et al., 2007), and thus is not further discussed here. This dimeric model formed by 12 TM α helices possesses

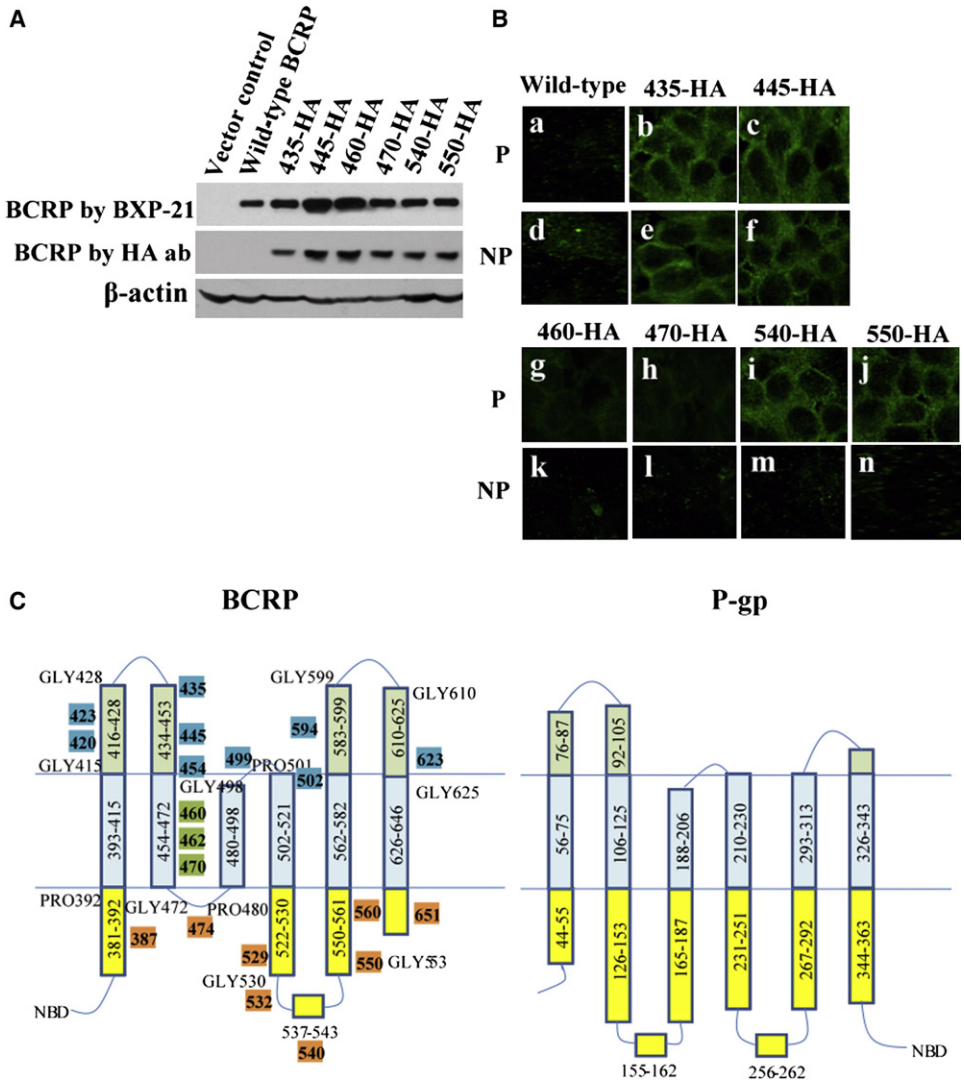

Figure 5. Analysis of Membrane Topology of BCRP by HA Tag Insertion and Immunofluorescence Confocal Microscopy as well as the Topology Model of BCRP

(A) Immunoblots of whole cell lysates of HEK cells transfected with wild-type BCRP and HA-tagged BCRP mutant cDNA constructs 435-HA, 445-HA, 460-HA, 470-HA, 540-HA, and 550-HA. Whole cell lysates (30 μg protein each lane) were immunoblotted, and BCRP was detected with the BCRP-specific antibody BXP-21 or a HA tag-specific antibody. β-actin expression was examined as an internal control. The vector control, wild-type BCRP, and the mutant constructs are indicated above the blots.

(B) Immunofluorescence confocal micrographs. HEK cells were transiently transfected with wild-type BCRP and HA-tagged BCRP mutant cDNAs, probed with the HA tag-specific antibody, and processed for fluorescence confocal microscopy. The HA-tagged BCRP signals are indicated in green. Exposure times were identical for all the micrographs. The HA tags in constructs 435-HA (b, e) and 445-HA (c, f) were detected in both permeabilized (P) and intact, non-permeabilized (NP) cells, whereas the HA tags in constructs 460-HA (g, k), 470-HA (h, l), 540-HA (i, m), and 550-HA (j, n) were detected only in permeabilized cells. The corresponding mutant constructs are shown above the micrographs. Wild-type BCRP (a, d) was analyzed as a control. The experiments were repeated twice, and similar results were obtained.

(C) The experimentally determined topology structure of BCRP as compared with that of mouse P-gp observed in its X-ray structure. Residues 387, 474, 529, 532, 540, 550, 560, and 651, and residues 420, 423, 435, 445, 454, 499, 502, 594, and 623 of BCRP were localized experimentally to the intracellular and extracellular loops, respectively. Residues 460, 462, and 470 were localized in the TM2 segment. Similar to the template structures, most of the TM α helices of BCRP start and/or end with glycine (GLY) or proline (PRO) as indicated. The length of TM α helices is indicated with the amino acid sequence numbers. The topologies of BCRP and P-gp are similar, except that the intracellular loop connecting TM2 and TM3 is missing in BCRP and the extracellular loop connecting TM5 and TM6 of BCRP is significantly larger than the corresponding region in P-gp.

a wide open inward-facing structure that is closed from the extracellular side. The entry of this open nucleotide-free structure is large enough to allow access of a bulky of BCRP substrates from either the inner leaflet or cytoplasm. Substrate-binding sites are likely located in the central cavity surrounded by TM α helices. TM α helices are connected by long intracellular or extracellular loops and extend far beyond the membrane interface with the only exception of TM3. The

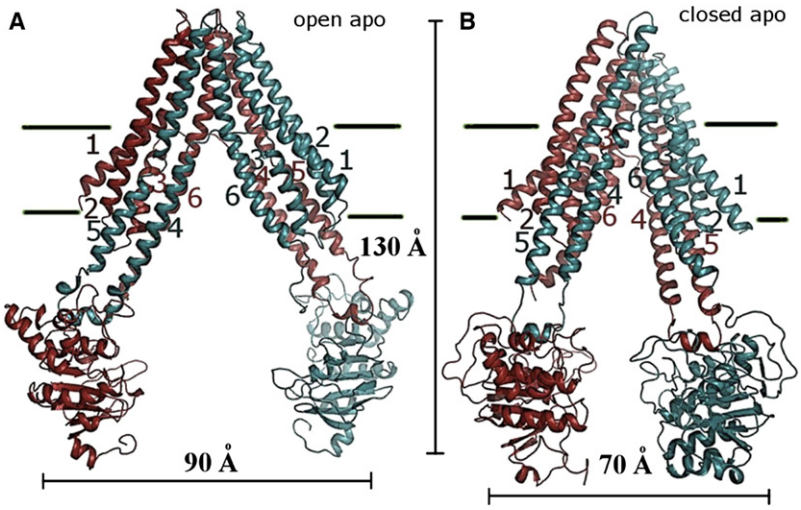

Figure 6. Homology Models of BCRP in the Open (A) and Closed (B) Apo Inward-Facing Nucleotide-free Apo Conformations

The models (A) and (B) were developed using the X-ray structures of MsbA from *E. coli* and mouse P-gp as the templates, respectively, as described. The open and closed apo inward-facing structures represent a substrate-free state and a substrate-bound state, respectively. The TM α helices of each BCRP monomer are labeled with numbers 1–6 in different colors. Individual BCRP monomer is shown in red or blue. The putative boundaries of the lipid bilayer are indicated with straight lines. A coupling helix in the intracellular loop connecting TM4 and TM5 of one BCRP monomer interacts with the NBD of the opposite monomer. The dimensions of one BCRP monomer are presented. See also Figure S3.

extracellular loop connecting TM1 and TM2 forms intermonomer contacts with residues in the extracellular loop connecting TM5 and TM6, and thus may contribute to stabilization of the dimeric structure. In addition, intermonomer interactions between the extracellular ends of the two centrally localized TM6 segments can be seen, similar to that observed for P-gp in cross-linking studies (Loo et al., 2003; Loo and Clarke, 1997). The unique feature of this BCRP model (Figure 6A) is the missing of the coupling helix 1 in the intracellular loop connecting TM 2 and TM3, which is present in all of the available template structures and could play a crucial role in the interactions between the NBD and the TMD of the same monomer. The first 18 residues at the NH_2-terminus and residues 285–380 in the putative linker region connecting the NBD to the TMD of BCRP could not be modeled due to the lack of appropriate templates. This linker region of BCRP is much longer than those of other ABC efflux transporters and may serve as the coupling helix 1. Another common feature that was revealed in the X-ray structures of Sav1866, MsbA, and P-gp is that a second coupling helix (coupling helix 2) crosses over and associates with the NBD of the opposite monomer. This crossover motif is also present in the homology model in the intracellular loop connecting TM4 and TM5, which may define the relative orientation of individual domains and allow flexibility in the transporter (Figure 6A). Glycine 553 in this region may be important for BCRP dimerization (Polgar et al., 2006). Similar wide-open apo inward-facing conformations have been shown in structures of other ABC transporters (Chami et al., 2002; Hofacker et al., 2007; Ward et al., 2007).

The second homology model of BCRP (Figure 6B) was developed based on the substrate-bound nucleotide-free structure of mouse P-gp (PDB code: 3G60) (Aller et al., 2009). This model represents the closed apo nucleotide-free inward-facing conformation of BCRP that likely occurs in the catalytic cycle after substrates enter the wide-open apo inward-facing conformation. Comparing the open and closed nucleotide-free models, we found that TM4 and TM5 of BCRP rotate ~30° with a rotation center at the extracellular side of the TMD near the putative substrate-binding cavity. This rigid body motion is possibly transmitted to the NBDs by the coupling helix 2 and forces the NBDs to close the wide-open entry from the intracellular side. The distance between the two NBDs in the closed apo nucleotide-free conformation, although becomes much shorter, still does not allow direct interactions of the NBDs with each other. The rotation also forces TMs 1 – 3 and 6 to similarly change their positions. These conformational changes result in an intracellular entry between the two TMDs in the closed apo structure which is ~20 Å narrower (a reduction from 90 Å to 70 Å) as compared with the open apo structure (Figure 6). Such a domain rearrangement would alter the shape of the substrate-binding cavity which is formed primarily by residues in the TMs by making it more compact, thus allowing interactions of substrates with both monomers at the same time. The results of homology modeling are consistent with our experimental data of electron crystallography. First, our EM data also demonstrated a similar rotation of the projection structure of BCRP in the presence of mitoxantrone (Figure 4). Second, such rotation also resulted in a closer packing of the BCRP molecules in the presence of mitoxantrone (Table 1). Taken together, both the EM data and homology modeling suggest that the BCRP dimer could become more compact upon substrate binding.

We further examined if the homology models of BCRP can match with the densities in the corresponding projection maps. This was performed by aligning two BCRP dimers of the models related by a two-fold screw axis, which correspond to the $p12_1$ plane group symmetry of the 2D crystals, with the EM maps using the Chimera program. In the drug-bound map, the TM α helices align well with the high-density regions (Figures 7A–7D). In the drug-free map, the larger tilt angles of TM α helices appear to cause densities with more elongated areas (Figures 7E–7H). In both maps, two BCRP dimers cover the whole unit cell. It is worth noting that the dimerization pattern of the open apo model (Figure 7E–H) is similar to the oligomeric structure of the open apo form of MsbA resolved in its X-ray crystal structure (Ward et al., 2007) (PDB code 3B5W). Overall, the fitting again suggests that our EM data and homology modeling appear to be in good agreement. The fitting supports the crystallographic data that the asymmetric unit cell in both

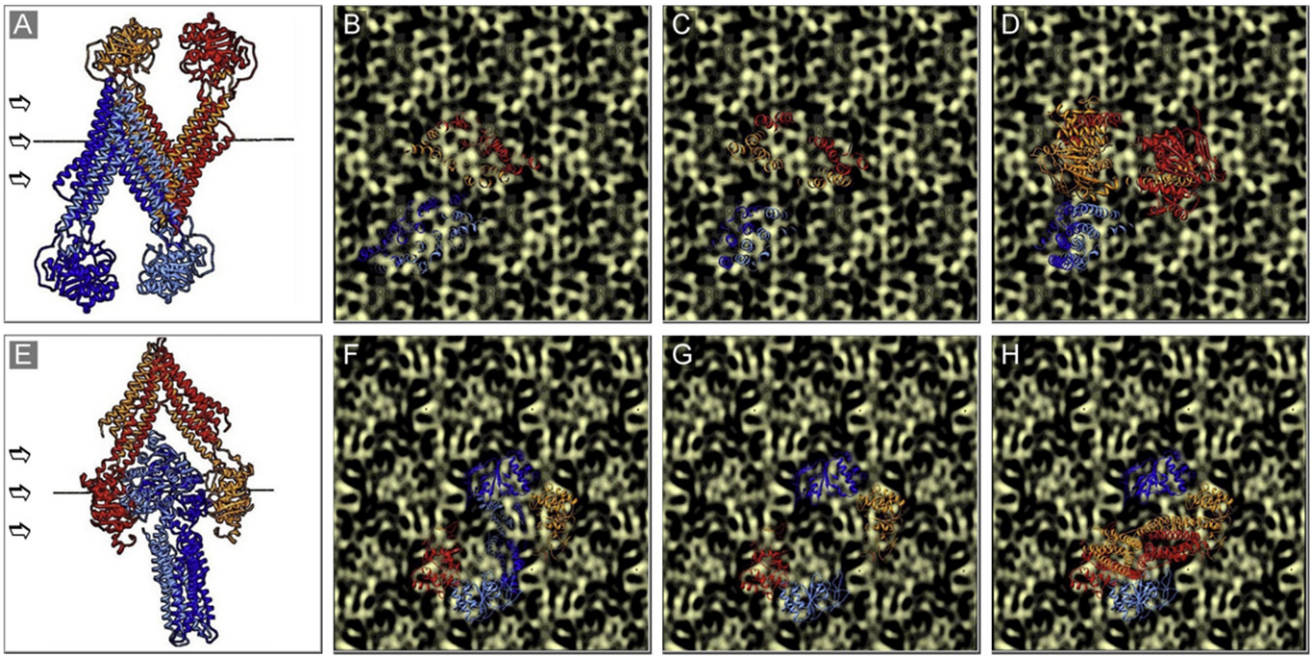

Figure 7. Alignment of the BCRP Models with Projection Maps

(A) Two BCRP dimers of the closed apo model are related by a two-fold screw axis, corresponding to the $p12_1$ plane group symmetry of the 2D crystals in the presence of mitoxantrone.

(B–D) A view of the fit of the two BCRP dimers in one unit cell of the projection map in the presence of mitoxantrone, from the bottom, the center, and the top of the fit, respectively.

(E) Two BCRP dimers of the open apo model are related by a two-fold screw axis, corresponding to the $p12_1$ plane group symmetry of the 2D crystals in the absence of mitoxantrone.

(F–H) A view of the fit of the two BCRP dimers in one unit cell of the projection map in the absence of mitoxantrone, from the bottom, the center, and the top of the fit, respectively.

projection maps may accommodate two BCRP dimers. Individual secondary structure elements (e.g., 12 TM α helices) may not be clearly defined in the 2D projection maps. This is because the BCRP molecule is not reconstituted in lipid and we are uncertain whether the molecule is perpendicular to the crystal plane. Also, in cryo projection maps, TM α helices, NBDs, and underlying loops will be superimposed in the structure (Kuo et al., 2005). Hence, only the overall densities and shape of the BCRP models could be rationalized in the projection maps by the fitting. For the same reasons, we did not try to improve the models by such fitting as this would require a 3D map.

In conclusion, in the present study, we have described the successful crystallization of the first well-diffracting 2D crystals of BCRP at a resolution that provides significant structural information. For the first time, we demonstrated the conformational change of BCRP in the presence of its substrate drug, mitoxantrone. Homology modeling helped interpret the structural data. Our results are consistent with most of the biochemical data available for BCRP. These structural data enhance our understanding of the drug binding and transport mechanism of BCRP and establish a basis for further structure-function analyses of this important drug transporter. The exact number of TM α helices, and their relative orientations and assignment in the protein sequence, cannot be resolved from the projection structures. This will require the calculation of a 3D map, which is currently underway.

EXPERIMENTAL PROCEDURES

Expression and Purification of BCRP in *Pichia pastoris*

Expression of BCRP in *Pichia pastoris* was carried out as previously described (Mao et al., 2004; Wu et al., 2005). Further details for expression and purification of BCRP are described in the Supplemental Experimental Procedures.

Measurement of BCRP ATPase Activity

ATPase activity of purified BCRP was measured as described (Mao et al., 2004). Further details can be found in the Supplemental Experimental Procedures.

Two-Dimensional Crystallization, Electron Microscopy, and Imaging Processing

The 2D crystals of BCRP were prepared essentially the same as previously described (Rosenberg et al., 2005). BCRP (~0.03 mg/ml) was incubated with a mixture containing 10% (w/v) polyethylene glycol 4000, 100 mM ammonium sulfate, 0.1% (w/v) DDM in Tris-HCl buffer (pH 7.4) with and without 5 mM mitoxantrone for 17 hr at 4°C. The sample was incubated with 300 mesh gold or molybdenum grids coated with continuous carbon (TAAB Laboratories Equipment Ltd, Berkshire, UK). The crystallization experiments were evaluated by electron microscopy following negative staining in 2% (w/v) uranyl acetate. The use of heavy metal gold or molybdenum grids is unlikely to have changed the conformation of the protein because both were used for non-mitoxantrone bound and mitoxantrone bound, and thus if they were eliciting an effect, we would have seen this for the non-mitoxantrone-bound experiments. We saw no additional conformational changes using a gold grid instead of a molybdenum grid and vice versa. Some specimens were frozen in liquid ethane and subsequently transferred to a cryoholder cooled by liquid N_2 to a temperature of approximately −175°C. Images were collected on a Tecnai F20

field-emission microscope at the University of Leeds at 200 keV at liquid N_2 temperatures, magnification of 50,000 ×, and mean underfocus ranging from 4,000 to 15,000 Å. Images were also collected on a FEI Tecnai G2 Polara microscope (300 keV) at the University of Manchester with a Gatan CCD camera and a CM200 at 200 keV equipped with a Tietz CCD camera at Imperial College, London. Images were recorded at 10–12 e/Å^2. Images were recorded on Kodak SO-163 film and developed for 12 min in a full-strength Kodak D19 developer or recorded on CCD camera. We used the methods described in the Supplemental Information to do the image processing with MRC and 2 dx software (Crowther et al., 1996; Gipson et al., 2006).

Determination of Membrane Topology of BCRP by Epitope Insertion and Immunofluorescence

HA-tagged BCRP mutants with the HA (YPYDVPDYA) tags inserted, one at a time, at positions immediately following the residues 435, 445, 460, 470, 540, and 550 were generated by epitope insertion mutagenesis. The pcDNA3.1 constructs containing HA-tagged BCRP mutant cDNAs were confirmed by DNA sequencing and used for transient transfection into HEK293 cells. Expression of HA-tagged BCRP mutants was then analyzed by immunoblotting using the BCRP-specific antibody BXP-21 and the antibody against the HA tag. The efflux activity of HA-tagged BCRP mutants and the location of the HA tags with respect to the plasma membrane (intracellular or extracellular) were determined using a flow cytometric efflux assay and immunofluorescence confocal microscopy, respectively. When permeabilization of cells was needed, 0.01% (v/v) Triton X-100 was used. All the above methods were essentially the same as previously described (Wang et al., 2008).

Homology Modeling of BCRP

Based on the topology structure we determined (Wang et al., 2008), we performed homology modeling to generate the open and closed apo nucleotide-free conformations of BCRP. Primary sequence of human BCRP was taken from the Universal Protein Resource (http://www.uniprot.org, accession code: Q9UNQ0). Crystal structures of templates were obtained from the Brookhaven Protein Data Bank (http://www.rcsb.org/). The closed substrate-bound inward-facing form of mouse P-gp (Aller et al., 2009) (PDB code: 3G60) and the open substrate-unbound inward-facing form of MsbA (Ward et al., 2007) (PDB code: 3B5W) (both are nucleotide-free) were used as full-length templates. MsbA was used as the template of the open substrate-unbound inward-facing conformation of BCRP because the P-gp structure in such a conformation has not been resolved. The topology of the outward-facing nucleotide-bound form of Sav1866 (Dawson and Locher, 2006) (PDB code: 2HYD) was also used in the refinement of sequence alignment. TM boundaries of the templates used in sequence alignment were derived from X-ray structures of the respective transporters. Two homology models of BCRP were built with one representing the substrate-free open apo inward-facing conformation based on MsbA and the other representing the substrate-bound closed apo inward-facing conformation based on the mouse P-gp structure. Further details can be found in the Supplemental Experimental Procedures.

SUPPLEMENTAL INFORMATION

Supplemental Information includes three figures and Supplemental Experimental Procedures and can be found with this article online at doi:10.1016/j.str.2010.01.017.

ACKNOWLEDGMENTS

We thank Karl Kadler, Alan Rosen, Roger Meadows, Les Lockey (The University of Manchester), John Trinick and Peiyi Wang (University of Leeds), Marin Van Heel, Tilliman Pape, and Raffa Carzaniga (Imperial College, London) for access and assistance with the respective microscopes. We thank Vinzenz Unger (Yale University), Anchi Cheng (Scripps Research Institute, San Diego, CA), and Linus Johannissen (The University of Manchester) for calculation of the phase quality plot, assistance with image processing, and the help in writing code, respectively. We acknowledge Honggang Wang (University of Washington) for technical assistance with confocal microscopy. We would also like to thank Catherine Vénien-Bryan (University of Oxford) for useful discussions, and the Cystic Fibrosis Foundation (USA) for a travel grant (to M.F.R.) for attendance at the 2dx meeting in California in 2008. This work was supported by the Leukemia Research Fund, London (to M.F.R.), a VIP Fellowship from the Wellcome Trust (to M.F.R.), in part by Grant 081406/Z/06/Z from the Wellcome Trust, and by the NIH grant GM073715 (to Q.M.). This work is dedicated in memory of Anne-Marie Buckle (The University of Manchester).

Received: September 23, 2009
Revised: December 10, 2009
Accepted: January 22, 2010
Published: April 13, 2010

REFERENCES

Aller, S.G., Yu, J., Ward, A., Weng, Y., Chittaboina, S., Zhuo, R., Harrell, P.M., Trinh, Y.T., Zhang, Q., Urbatsch, I.L., and Chang, G. (2009). Structure of P-glycoprotein reveals a molecular basis for poly-specific drug binding. Science *323*, 1718–1722.

Appel, M., Hizlan, D., Vinothkumar, K.R., Ziegler, C., and Kuhlbrandt, W. (2009). Conformations of NhaA, the Na+/H+ exchanger from Escherichia coli, in the pH-activated and ion-translocating states. J. Mol. Biol. *388*, 659–672.

Chami, M., Steinfels, E., Orelle, C., Jault, J.M., Di Pietro, A., Rigaud, J.L., and Marco, S. (2002). Three-dimensional structure by cryo-electron microscopy of YvcC, an homodimeric ATP-binding cassette transporter from Bacillus subtilis. J. Mol. Biol. *315*, 1075–1085.

Collaborative Computational Project, Number 4 (CCP4). (1994). The CCP4 suite: programs for protein crystallography. Acta Crystallogr. D Biol. Crystallogr. *50*, 760–763.

Crowther, R.A., Henderson, R., and Smith, J.M. (1996). MRC image processing programs. J. Struct. Biol. *116*, 9–16.

Dawson, R.J., and Locher, K.P. (2006). Structure of a bacterial multidrug ABC transporter. Nature *443*, 180–185.

Gipson, B., Zeng, X., and Stahlberg, H. (2006). 2dx_merge: data management and merging for 2D crystal images. J. Struct. Biol. *160*, 375–384.

Glavinas, H., Kis, E., Pal, A., Kovacs, R., Jani, M., Vagi, E., Molnar, E., Bansaghi, S., Kele, Z., Janaky, T., et al. (2007). ABCG2 (breast cancer resistance protein/mitoxantrone resistance-associated protein) ATPase assay: a useful tool to detect drug-transporter interactions. Drug Metab. Dispos. *35*, 1533–1542.

Gonen, T., Cheng, Y., Sliz, P., Hiroaki, Y., Fujiyoshi, Y., Harrison, S.C., and Walz, T. (2005). Lipid-protein interactions in double-layered two-dimensional AQP0 crystals. Nature *438*, 633–638.

Hazai, E., and Bikadi, Z. (2008). Homology modeling of breast cancer resistance protein (ABCG2). J. Struct. Biol. *162*, 63–74.

Henderson, R., Baldwin, J.M., Downing, K.H., Lepault, J., and Zemlin, F. (1986). Structure of purple membrane from Halobacterium halobium - recording, measurement and evaluation of electron-micrographs at 3.5 A resolution. Ultramicroscopy *19*, 147–178.

Hofacker, M., Gompf, S., Zutz, A., Presenti, C., Haase, W., van der Does, C., Model, K., and Tampe, R. (2007). Structural and functional fingerprint of the mitochondrial ATP-binding cassette transporter Mdl1 from Saccharomyces cerevisiae. J. Biol. Chem. *282*, 3951–3961.

Holm, P.J., Bhakat, P., Jegerschold, C., Gyobu, N., Mitsuoka, K., Fujiyoshi, Y., Morgenstern, R., and Hebert, H. (2006). Structural basis for detoxification and oxidative stress protection in membranes. J. Mol. Biol. *360*, 934–945.

Honjo, Y., Hrycyna, C.A., Yan, Q.W., Medina-Perez, W.Y., Robey, R.W., van de Laar, A., Litman, T., Dean, M., and Bates, S.E. (2001). Acquired mutations in the MXR/BCRP/ABCP gene alter substrate specificity in MXR/BCRP/ABCP-overexpressing cells. Cancer Res. *61*, 6635–6639.

Kuhlbrandt, W., Wang, D.N., and Fujiyoshi, Y. (1994). Atomic model of plant light-harvesting complex by electron crystallography. Nature *367*, 614–621.

 ©2010 Elsevier Ltd All rights reserved

Kuo, A., Domene, C., Johnson, L.N., Doyle, D.A., and Venien-Bryan, C. (2005). Two different conformational states of the KirBac3.1 potassium channel revealed by electron crystallography. Structure *13*, 1463–1472.

Larue, K., Kimber, M.S., Ford, R., and Whitfield, C. (2009). Biochemical and structural analysis of bacterial O-antigen chain length regulator proteins reveals a conserved quaternary structure. J. Biol. Chem. *284*, 7395–7403.

Li, Y.F., Polgar, O., Okada, M., Esser, L., Bates, S.E., and Xia, D. (2007). Towards understanding the mechanism of action of the multidrug resistance-linked half-ABC transporter ABCG2: a molecular modeling study. J. Mol. Graph. Model *25*, 837–851.

Loo, T.W., Bartlett, M.C., and Clarke, D.M. (2003). Simultaneous binding of two different drugs in the binding pocket of the human multidrug resistance P-glycoprotein. J. Biol. Chem. *278*, 39706–39710.

Loo, T.W., and Clarke, D.M. (1997). Drug-stimulated ATPase activity of human P-glycoprotein requires movement between transmembrane segments 6 and 12. J. Biol. Chem. *272*, 20986–20989.

Loo, T.W., and Clarke, D.M. (2001). Defining the drug-binding site in the human multidrug resistance P-glycoprotein using a methanethiosulfonate analog of verapamil, MTS-verapamil. J. Biol. Chem. *276*, 14972–14979.

Maliepaard, M., Scheffer, G.L., Faneyte, I.F., van Gastelen, M.A., Pijnenborg, A.C., Schinkel, A.H., van De Vijver, M.J., Scheper, R.J., and Schellens, J.H. (2001). Subcellular localization and distribution of the breast cancer resistance protein transporter in normal human tissues. Cancer Res. *61*, 3458–3464.

Mao, Q., Conseil, G., Gupta, A., Cole, S.P., and Unadkat, J.D. (2004). Functional expression of the human breast cancer resistance protein in Pichia pastoris. Biochem. Biophys. Res. Commun. *320*, 730–737.

Mao, Q., and Unadkat, J.D. (2005). Role of the breast cancer resistance protein (ABCG2) in drug transport. AAPS J. *7*, E118–E133.

McDevitt, C.A., Collins, R.F., Conway, M., Modok, S., Storm, J., Kerr, I.D., Ford, R.C., and Callaghan, R. (2006). Purification and 3D structural analysis of oligomeric human multidrug transporter ABCG2. Structure *14*, 1623–1632.

Murata, K., Mitsuoka, K., Hirai, T., Walz, T., Agre, P., Heymann, J.B., Engel, A., and Fujiyoshi, Y. (2000). Structural determinants of water permeation through aquaporin-1. Nature *407*, 599–605.

Ozvegy-Laczka, C., Koblos, G., Sarkadi, B., and Varadi, A. (2005). Single amino acid (482) variants of the ABCG2 multidrug transporter: major differences in transport capacity and substrate recognition. Biochim. Biophys. Acta *1668*, 53–63.

Polgar, O., Ozvegy-Laczka, C., Robey, R.W., Morisaki, K., Okada, M., Tamaki, A., Koblos, G., Elkind, N.B., Ward, Y., Dean, M., et al. (2006). Mutational studies of G553 in TM5 of ABCG2: a residue potentially involved in dimerization. Biochemistry *45*, 5251–5260.

Polgar, O., Robey, R.W., and Bates, S.E. (2008). ABCG2: structure, function and role in drug response. Expert Opin. Drug Metab. Toxicol. *4*, 1–15.

Pozza, A., Perez-Victoria, J.M., Sardo, A., Ahmed-Belkacem, A., and Di Pietro, A. (2006). Purification of breast cancer resistance protein ABCG2 and role of arginine-482. Cell. Mol. Life Sci. *63*, 1912–1922.

Robey, R.W., To, K.K., Polgar, O., Dohse, M., Fetsch, P., Dean, M., and Bates, S.E. (2009). ABCG2: a perspective. Adv. Drug Deliv. Rev. *61*, 3–13.

Rosenberg, M.F., Kamis, A.B., Callaghan, R., Higgins, C.F., and Ford, R.C. (2003). Three-dimensional structures of the mammalian multidrug resistance P-glycoprotein demonstrate major conformational changes in the transmembrane domains upon nucleotide binding. J. Biol. Chem. *278*, 8294–8299.

Rosenberg, M.F., Kamis, A.B., Aleksandrov, L.A., Ford, R.C., and Riordan, J.R. (2004). Purification and crystallization of the cystic fibrosis transmembrane conductance regulator (CFTR). J. Biol. Chem. *279*, 39051–39057.

Rosenberg, M.F., Callaghan, R., Modok, S., Higgins, C.F., and Ford, R.C. (2005). Three-dimensional structure of P-glycoprotein: the transmembrane regions adopt an asymmetric configuration in the nucleotide-bound state. J. Biol. Chem. *280*, 2857–2862.

Sarkadi, B., Homolya, L., Szakacs, G., and Varadi, A. (2006). Human multidrug resistance ABCB and ABCG transporters: participation in a chemoimmunity defense system. Physiol. Rev. *86*, 1179–1236.

Slotboom, D.J., Sobczak, I., Konings, W.N., and Lolkema, J.S. (1999). A conserved serine-rich stretch in the glutamate transporter family forms a substrate-sensitive reentrant loop. Proc. Natl. Acad. Sci. USA *96*, 14282–14287.

Valpuesta, J.M., Carrascosa, J.L., and Henderson, R. (1994). Analysis of electron microscope images and electron diffraction patterns of thin crystals of phi 29 connectors in ice. J. Mol. Biol. *240*, 281–287.

Wakabayashi, S., Pang, T., Su, X., and Shigekawa, M. (2000). A novel topology model of the human Na(+)/H(+) exchanger isoform 1. J. Biol. Chem. *275*, 7942–7949.

Wang, H., Lee, E.W., Cai, X., Ni, Z., Zhou, L., and Mao, Q. (2008). Membrane topology of the human breast cancer resistance protein (BCRP/ABCG2) determined by epitope insertion and immunofluorescence. Biochemistry *47*, 13778–13787.

Ward, A., Reyes, C.L., Yu, J., Roth, C.B., and Chang, G. (2007). Flexibility in the ABC transporter MsbA: Alternating access with a twist. Proc. Natl. Acad. Sci. USA *104*, 19005–19010.

Wu, P., Oleschuk, C.J., Mao, Q., Keller, B.O., Deeley, R.G., and Cole, S.P. (2005). Analysis of human multidrug resistance protein 1 (ABCC1) by matrix-assisted laser desorption ionization/time of flight mass spectrometry: toward identification of leukotriene C4 binding sites. Mol. Pharmacol. *68*, 1455–1465.

Xu, J., Liu, Y., Yang, Y., Bates, S., and Zhang, J.T. (2004). Characterization of oligomeric human half-ABC transporter ATP-binding cassette G2. J. Biol. Chem. *279*, 19781–19789.